ACS OMEGA

http://pubs.acs.org/journal/acsodf

Article

Single Crystal Investigations, Hirshfeld Surface Analysis, DFT Studies, Molecular Docking, Physico-Chemical Characterization, and Biological Activity of a Novel Non-Centrosymmetric Compound with a Copper Transition Metal Precursor

Afef Gannouni, Wiem Tahri, Thierry Roisnel, Saud I. Al-Resayes, Mohammad Azam,* and Riadh Kefi*

Cite This: *ACS Omega* 2023, 8, 7738−7748

Read Online

ACCESS | Metrics & More | Article Recommendations | Supporting Information

ABSTRACT: A novel organic−inorganic hybrid non-centrosymmetric superconductor material [2-ethylpiperazine tetrachlorocuprate(II)] has been synthesized and investigated by means of Fourier transform infrared spectroscopy, single-crystal X-ray crystallography, thermal analyses, and density functional theory (DFT) studies. The single-crystal X-ray analysis indicates that the studied compound crystallizes in the $P2_12_12_1$ orthorhombic space group. Hirshfeld surface analyses have been used to investigate non-covalent interactions. Organic cations $[C_6H_{16}N_2]^{2+}$ and inorganic moieties $[CuCl_4]^{2-}$ alternatively connect N−H···Cl and C−H···Cl hydrogen bonds. In addition, the energies of the frontier orbitals, highest occupied molecular orbital, lowest unoccupied molecular orbital, the reduced density gradient analyses and quantum theory of atoms in molecules analyses, and the natural bonding orbital are also studied. Furthermore, the optical absorption and photoluminescence properties were also explored. However, time-dependent/DFT computations were utilized to examine the photoluminescence and UV−vis absorption characteristics. Two different methods, 2, 2-diphenyl-1-picryhydrazyl radical and 2,2-azino-bis(3-ethylbenzothiazoline-6-sulfonic acid radical scavenging, were used to evaluate the antioxidant activity of the studied material. Furthermore, the title material was docked to the SARS-CoV-2 variant (B.1.1.529) in silico to study the non-covalent interaction of the cuprate(II) complex with active amino acids in the spike protein.

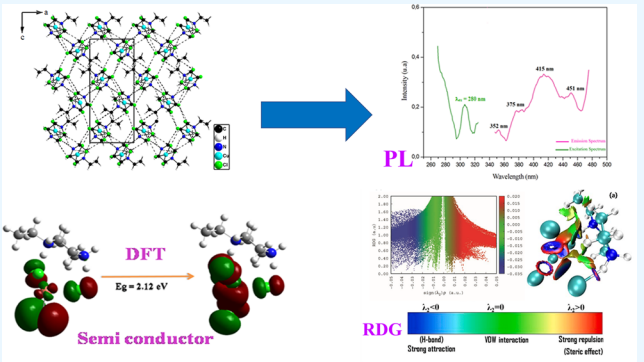

INTRODUCTION

Over the years, crystal engineering approaches to integrate the inherent features of organic and inorganic materials into one material have drawn significant interest in the design of organic−inorganic materials. The hydrogen bonds N−H···Cl and C−H···Cl dominate the cohesive forces in these hybrid materials. Copper is an alluring transition metal with a d^9 electron system and exhibits a wide range of coordination compounds, particularly with coordination numbers four, five, and six.[1−4] Moreover, Cu(II) complexes can be used for a variety of biological and catalytic applications.[5,6]

Piperazines and their derivatives have intriguing pharmacological, cardiovascular, and autonomic properties. In addition, it has a wide range of applications due to its combination of organic and inorganic molecules, considering their pharmacological, optical, thermal, biological, and electrical properties, including photocatalysis and medicine.[7−14] Furthermore, the piperazine derivatives are a group of strongly basic amines capable of forming dications with normally all NH bonds capable of forming H bonds and have been used in pharmacological substances in a variety of therapeutic fields including antidepressants, antibiotics, antifungal, anticancer, and antipsychotic drugs.[15]

Herein, we describe the synthesis and structure investigations of a new hybrid inorganic−organic material $(C_6H_{16}N_2)[CuCl_4]$, abbreviated as 2EPCU, based on the piperazine cation and Cu^{2+} metal ion. Hirshfeld surface analysis has been proposed to understand the various intermolecular interactions. In addition, vibrational, UV−vis optical absorption, and photoluminescence (PL) studies were also performed. Furthermore, theoretical investigations employing quantum theory atom in molecule (QTAIM), reduced density gradient (RDG), natural bond orbital (NBO), and molecular electrostatic potential were carried out to assess the structural topology. In addition, the antioxidative properties of

Received: November 17, 2022
Accepted: February 10, 2023
Published: February 17, 2023

https://doi.org/10.1021/acsomega.2c07389
ACS Omega 2023, 8, 7738−7748

the investigated material were also examined using the DPPH and ABTS radical scavenger methods.[16,17] Moreover, molecular docking studies were also conducted to cure illnesses caused by coronavirus. The SARS-CoV-2 main protease and its variant were obtained as a target. It is expected that the binding of metal ions to active sites could be lethal for different spike protein variants.[18−21] The findings reveal that the isolated material has significant potential in both the pharmaceutical and optical fields.

EXPERIMENTAL SECTION

Material and Methods. The infrared spectra were analyzed with a Nicolet IR 200 FT-IR spectrophotometer, which measures infrared wavelengths from 500 to 4000 cm^{-1} at room temperature, while a Perkin Elmer Lambda 35 UV/vis spectrophotometer was used to measure the absorption at room temperature at wavelength 200−1000 nm. The Perkin Elmer LS55 Spectrofluorometer was used to perform the PL analyses at room temperature.

Synthesis of $(C_6H_{16}N_2)[CuCl_4]$. $CuCl_2.2H_2O$ (47.58 mg, 0.2 mmol) dissolved in 10 mL of deionized water was added to a solution of (2-ethyl) piperazines (60.58 mg, 0.1 mmol) in 5.0 mL of deionized water containing 2 mL of strong hydrochloric acid (37%). After 30 min of stirring, a yellow color solution was obtained, which yielded beautiful yellow crystals suitable for X-ray diffraction on slow evaporation at room temperature. Yield 85%; Anal. calcd: C, 22.39%; N, 8.71%; Cl, 32.65%; Cu, 19.76%; (IR, KBr, cm^{-1}): $\nu_{(NH2)}$, 3036−2987; $\nu_{(NH)}$, 2751; $\nu_{(CH2)}$, 2790; $\nu_{(CH3)}$, 2722; (UV/vis, nm): 423, 650.

X-ray Single-Crystal Structural Analyses. X-ray diffraction studies were conducted on appropriate single crystals to determine the structure of the title compound. Crystallographic data were acquired using a (CMOS) PHOTON monochromated Mo-Kα radiation (λ = 0.71073 Å) on a D8 Venture diffractometer at 150 (2) K. A dual space algorithm in the SHELXT program[22] was used to solve the structure and refined using full-matrix least-squares techniques with the F2 SHELXL program[23] (CCDC-2069447). Anisotropic atomic displacement parameters were used to refine all non-hydrogen atoms. H atoms were eventually inserted in their calculated places and handled using appropriate riding models with restricted thermal parameters, excluding the hydrogen atom associated with nitrogen atom N6, which was incorporated into the structure using Fourier difference map analysis. A final refinement of $F2$ with 2961 unique intensities and 122 parameters converged at ωR ($F2$) = 0.0769 (RF = 0.0330) for 2758 observed reflections with ($I > 2\sigma$). Diamond[24] was utilized to make the drawings.

Quantum Chemical Calculations. The density functional theory (DFT/B3LYP)[25−27] at the LanL2DZ basis set was used to optimize the parameters of the non-centrosymmetric compound $(C_6H_{16}N_2)[CuCl_4]$ using the Gaussian 09 W program package.[28] The chosen cluster consists of a tetrahedral $[CuCl_4]^{2-}$ and an organic $[C_6H_{16}N_2]^{2+}$ cation. All parameters were relaxed, and all calculations resulted in an optimized geometry. Vibrational analysis calculations failed to show any fictitious modes, validating local minima. Potential energy distributions were used to interpret the theoretical vibrational spectra of the title compound using the VEDA4 program.[29] The calculations for the time-dependent (TD)-DFT were performed at a similar theoretical level. Vertical excitation energy and frontier molecular orbital methods have been used to investigate the optical characteristics of 2EPCU, specifically the intermolecular orbital interaction and the charge transfer event.

Molecular Docking. Molecular docking of the title compound with spike protein was performed using a demo version of Genetic Optimization for Ligand Docking (GOLD). A 3D crystal structure of SARS-CoV-2 spike protein coupled to angiotensin-converting enzyme 2 (ACE2) (PDB ID: 6M0J) with a resolution of 2.45 Å was downloaded from the Protein Data Bank to begin the docking study. The spike protein with the reference molecule associated with ACE2 was detached from the 3D structure of the receptor using Discovery studio[30] to perform an in-silico study. A CIF file of the 2EPCU was converted to an acceptable *mol2 format for use in docking processes. The Hermes visualize is an interface of the GOLD suite that was used to prepare the 3D structure of spike protein such as missing loops, side, and chains, adding hydrogen to amino acids, and deleting water. The position of the reference molecule coupled to the spike protein was used to confirm the active site for the spike protein. All other parameters were left at their default levels, and the complexes were subjected to 10 genetic algorithm runs using the GOLD Score fitness function. The best-docked pose obtained from the docking method was employed to visualize the interactions of the complex with the spike protein using the Discovery studio visualization.

In Vitro Antioxidant Study. The $DPPH^{\cdot+}$ and $ABTS^{\cdot+}$ assays were used to assess the antioxidant activity of 2EPCU. The $DPPH^{\cdot+}$ (2, 2-diphenyl-1-picryhydrazyl radical) assay was carried out using a slightly modified method developed by Dhieb et al.[31] The absorbance at 517 nm was set to 0.70 ± 0.020 after stirring for 40 min with a 0.1 mM $DPPH^{\cdot+}$ solution in methanol. Finally, 3 mL of the $DPPH^{\cdot+}$ solution was added to 100 μL of the diluted sample (10 to 50 $mg.mL^{-1}$ of varied concentration were) and the mixture was left to incubate for 30 min in the dark under aluminum foil. A Shimadzu UV−vis 160A spectrophotometer was used to measure the absorbance of the final solutions at 516 nm relative to the control solution (MeOH instead of extract in $DPPH^{\cdot+}$ solution). The antioxidant activity of the title compound was measured in terms of its ability to inhibit $DPPH^{\cdot+}$ radical by a percentage and determined using the following equation

$$DPPH^{\cdot+}\ \text{radicals scavenged activity}\ (\%) = [(A_0 - A_1)/A_0] \times 100$$

The absorbance values for the blank and the title compound are denoted by A_0 and A_1, respectively. Guesmi et al. revealed that it is possible to scavenge the $ABTS^{\cdot+}$ (2,2-azino-bis(3-ethylbenzothiazoline-6-sulfonic acid) using a modified method.[32] After 16 h of dark incubation (4 °C), the interaction of $ABTS^{\cdot+}$ (7 mM in 20 mM sodium acetate buffer, pH 4.5) with an oxidizing agent (2.45 mM potassium persulfate) results in a persistent, dark blue-green radical solution. The test reagent was prepared from a diluted solution with an absorbance of 0.7 ± 0.02 at 734 nm. The reaction mixture was supplemented with 20 μL of sample and 3 mL of reagent, and it was then incubated for half an hour at 30 °C in a water bath. The test solution becomes colorless when unpaired electrons in the sample are sequestered by antioxidants and the absorbance at 734 nm decreases. Three hundred microliters of a diluted sample at different concentrations (0.5 and 100 $mg.mL^{-1}$) was added to 3 mL of $ABTS^{\cdot+}$ working solution. Each mixture was shaken vigorously before incubating in the dark at room temperature for 6 min. Each supernatant's absorbance was

https://doi.org/10.1021/acsomega.2c07389
ACS Omega 2023, 8, 7738−7748

determined at 734 nm. The following equation was used to determine the percentage of $ABTS^{\cdot+}$ scavenged

$$ABTS^{\cdot+}\ \text{radical scavenging activity}\ (\%) = [(A_0 - A_1)/A_0] \times 100$$

where A_0 and A_1 stand for the absorbance of the reaction mixture before and after the addition of the test compound, respectively.

RESULTS AND DISCUSSION

X-ray Crystal Structure. The X-ray crystal structure analysis of $(C_6H_{16}N_2)[CuCl_4]$ reveals the complex to be crystallized in the orthorhombic space group $P2_12_12_1$ with the unit cell volume being 1292.2 Å (Table 1). The asymmetric unit is formed by one $[CuCl_4]^{2-}$ anion and one $[C_6H_{16}N_2]^{2+}$ cation, as depicted in (Figure 1). An analysis of the structure of 2-ethylpiperazin-1,4-ium tetrachloridocuprate(II) clearly demonstrates that the structural arrangement may be explained by an isolated $CuCl_4$ unit and organic groups through a network extremely rich in N−H···Cl and C−H···Cl hydrogen bonds. This type of arrangement creates tunnels bounded by eight groups (four anions and four cations), as shown in Figure 2a. According to the direction (Figure 2b), the same structure also produces tunnels, but this is time-limited by four entities (two anions and two cations). The N···Cl distances range from 3.164(4) to 3.412(4), while N−H ···Cl angle values range from 126.2° to 152.2°. The C···Cl distances range from 3.528(5) to 3.726(5), while C−H ···Cl angles range between 132.7° and 170.6° (Table 2).

Table 1. Refinement Details for $(C_6H_{16}N_2)[CuCl_4]$

crystal data	
chemical formula	$(C_6H_{16}N_2)[CuCl_4]$
crystal color	yellow
formula weight (g/mol)	321.55
crystal system	orthorhombic
space group	$P2_12_12_1$
a, *b*, *c* (Å)	7.4489 (8), 9.9144 (10), 17.4977 (16)
$\alpha = \beta = \gamma$ (°)	90
volume *V* (Å^3)	1292.2(2)
Z	4
crystal size (mm^3)	0.330 × 0.120 × 0.070
radiation (wavelength (Å))	0.71073
F (000)	652
density (calculated), (mg/m^3)	1.653
diffractometer	D8 venture diffractometer
theta range for data collection (°)	2.361−27.483
reflections collected	7813
index ranges	**h** = −9/9; **k** = −12/12; **l** = −20/22
no. of measured, independent &	2961
observed [$I > 2\ s(I)$] reflections	2758
absorption coefficient/[mm^{-1}]	2.479
abs. correction	multi-scan
max and min. Transmission	0.841 and 0,662
goodness-of-fit on F^2	1.074
final *R* indices [$I > 2\ s(I)$]	*R*1 = 0.0330, *wR*2 = 0.0769
R indices [all data]	*R*1 = 0.0380, *wR*2 = 0.0796
largest diff. Peak and hole [e Å^3]	−0.566, 0.435

In addition, the inorganic anion has a tetrahedral structure with four chlorine atoms $[CuCl_4]^{2-}$ bonded to a copper atom (Cu25). Cu25−Cl bond lengths range from 2.2253(13) to 2.2670(14) Å, while the Cl−Cu25−Cl bond angles range between 95.67(5) and 142.47(5)°. These bond distances and angles of the $CuCl_4^{2-}$ anion are consistently found in other compounds.[33,34] Mean distortion indices and angles in $[CuCl_4]$ were calculated to be 0.0104 for Cu25−Cl and 0.1548 for Cl−Cu25−Cl and were described using the Baur technique.[35] These values show the disphenoidal geometry for $CuCl_4$. In addition, the examination of the organic entity 2-ethylpiperazine-1,4-ium shows interatomic distances C−C and N−C between 1.505 (7)−1.509 (6) and 1.490 (6)−1.504 (6), respectively. The values of the N-C-C angles range from 109.4 (4) to 113.0 (5)° and those of C−N−C angles are between 110.4 (4)° and 110.9 (4)°. All bond angles and distances are of the same order of magnitude as those found in hybrid compounds containing piperazine derivatives.[36−40] Table 3 summarizes the most important experimental and theoretical geometrical properties of 2EPCU units. The analyses of organic cation show that the piperazine fragment is cyclic and it has the best puckering chair conformation: *q*1 = 0.5966 Å; *q*2 = 0.1946 Å; *q*3 = 0.5966; θ = 19.04°; and φ2 = − 121.99° and φ3 = −104.67.[41]

Hirshfeld Surface Analyses. Hirshfeld surface analyses were performed on $(C_6H_{16}N_2)[CuCl_4]$ to investigate the role of the organic base in structure propagation. Crystal Explorer 3.1[42] was used to compute the Hirshfeld surface. d_{norm} can be calculated as follows[43,44]

$$d_{norm} = (di - ri^{vdw})/ri^{vdw} + (de - re^{vdw})/re^{vdw}$$

where ri^{vdw} and re^{vdw} represent the Van der Waals radii of the atoms inside or outside the surface, respectively, while di and de are the separations between the closest atoms inside and outside the surface. The 3D d_{norm} surfaces enable the identification of previously characterized contacts between the organic $[C_6H_{16}N_2]^{2+}$ and inorganic $[CuCl_4]^{2-}$ units. The enormous circular depressions (deep red) can be seen on the Hirshfeld surface of the asymmetric unit mapped with the d_{norm} property. These depressions are evidence of hydrogen bonding contacts resulting from the N−H ···Cl and C−H ···Cl interactions (Figure 3). The d_e and d_i distance scales were shown as the default view for the 2D fingerprint plots on the plot axes generated by the Hirshfeld surface analysis. Cl···H and H···H interactions dominated the crystal packing (66.4 and 27.1%, respectively) (Figure S1).

These interactions are attributed to hydrogen bonds, N−H···Cl and C−H···Cl at the cation $[C_6H_{16}N_2]^{+2}$ and anion $[CuCl_4]^{-2}$ in the asymmetric unit, respectively. The enrichment ratio (*E*) was used to examine the numerous intermolecular interactions occurring during the packaging of the crystal formation of the title compound. The enrichment ratio of an element pair is described as the ratio between the proportion of actual contacts in 2EPCU (% *C*) and the theoretical proportion of random contacts (% *R*).[45] As a result, the Cl−H contacts, which account for 66.4% of the Hirshfeld area, have the highest enrichment ratio *E* = 61.25. Therefore, Cl···H drives the molecular arrangement, which is made up of N−H···Cl and C−H···Cl types of hydrogen bonds. The percentages of Cu−H interactions (3.7%) are not significant, and the largest enrichment ratio *E* = 6.446 shows a modest over-representation. Furthermore, the H···H contact which has an *E* = 0.70 deviates from the Jelsch expectation.[46] It turns out that van der Waals forces have a significant impact on the packing stabilization in $(C_6H_{16}N_2)[CuCl_4]$. The electrostatic interactions between two chlorine atoms are repulsive in the

https://doi.org/10.1021/acsomega.2c07389
ACS Omega 2023, 8, 7738−7748

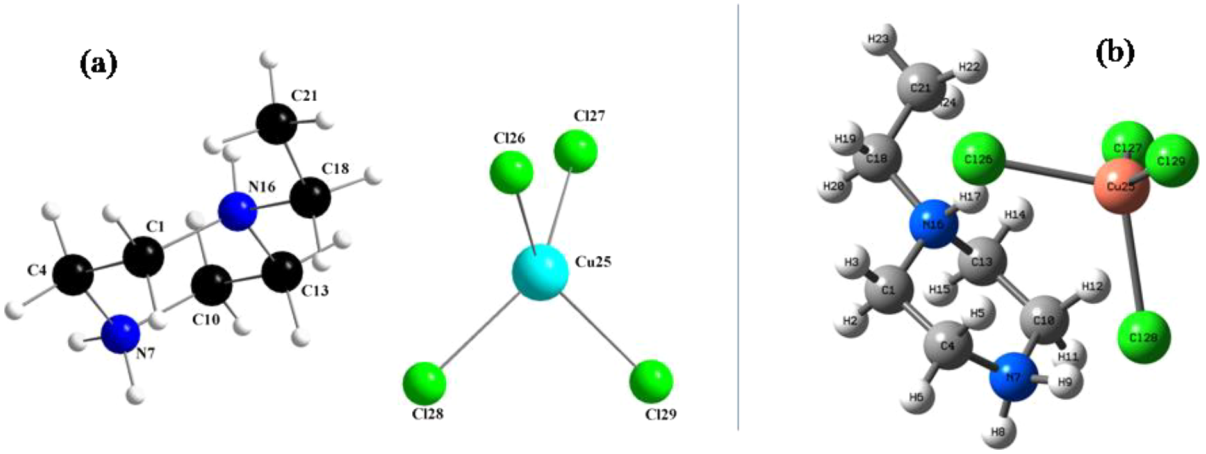

Figure 1. (a) Asymmetric unit with atom labeling and (b) optimized structure used in theoretical studies.

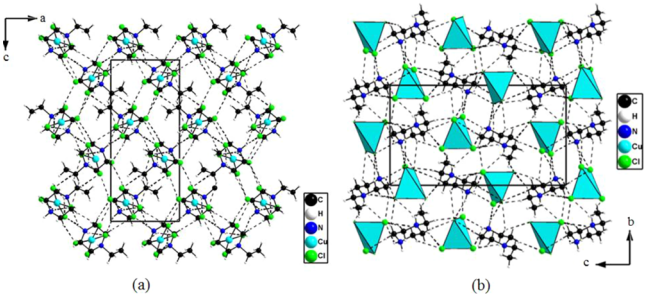

Figure 2. (a) Projection along the *b*-axis and (b) projection of the *a*-axis of $(C_6H_{16}N_2)[CuCl_4]$. Hydrogen bonds are indicated by dotted lines.

Cl−Cl (1.3%) with a weak enrichment ratio E = 0.107. The random contacts and enrichment ratios of $(C_6H_{16}N_2)[CuCl_4]$ generated from Hirshfeld contact surfaces (HS) are listed in Table 4.

Vibrational Analyses. IR absorption spectroscopy was performed to get more information about the structure of $(C_6H_{16}N_2)[CuCl_4]$ and to more accurately assign its vibrational modes on the basis of theoretical calculations (DFT) and previous findings reported by the literature for similar compounds.[1,47] Figure S2 shows the experimental (a) and theoretical (b) infrared spectra. In addition, IR vibrational modes are presented in Table S1 and are mostly based on theoretical results. Four absorption bands in the 3500−2500 cm^{-1} regions of the Fourier transform infrared spectroscopy spectrum are attributed to the symmetric and asymmetric vibrational modes $\nu_{(NH2)}$, $\nu_{(NH)}$, $\nu_{(CH2)}$, and $\nu_{(CH3)}$. These vibrational modes confirm that the hydrogen bonds decrease the strength of the bonds and lower their wave number. Moreover, the peaks located between 1625 and 1414 cm^{-1} are due to the deformation vibrations δ_s(NH2), δ_s(NH), δ_s(CH_2), δ_{as}(CH_2), and δ_s(HCC). The bands at 1421 and 1290 cm^{-1} are assigned to the vibrations τ_s(HCCN) and δ_{as}(HCC), respectively. Furthermore, the bands observed at 1119 and 1106 cm^{-1} can be assigned to C−C and C−N vibrations. The positions and their assignments for other peaks are 1023 cm^{-1} τ_s(NCCN), 1030 cm^{-1} τ_{as}(CCNC), 920 cm^{-1} τ_s(HNCC), and 800 cm^{-1} τ_{as}(HCNC). The symmetric and asymmetric stretching of CCN is observed between 900 and 470. The bands between 300 and 250 cm^{-1} corresponded to ν_s(CuCl), τ_s(HNCC), τ_s(HNHCl), and τ_s(NCCN). The deformation vibrations to CuClH, ClHN, and ClCuCl located in the range 220−100 cm^{-1}. Finally, the bands at 100 and 43 cm^{-1} are attributed to τ_s(CNCC), τ_s(CNHCl), and τ_s(CCNC). The various bands can be assign7ed by comparing them with those of similar materials in the literature.[48,49] It is evident from the correlation diagram in Figure S3 that there is a strong correlation between observed and calculated vibrational frequencies (the calculated coefficient of correlation (R) is 0.99453).

Optical Study. The compound $(C_6H_{16}N_2)[CuCl_4]$ shows a broad optical absorption at 200−1000 nm. Figure S4 shows the calculated and experimental absorption spectra for the

Table 2. Hydrogen Bonding Parameters (Å, °) for $(C_6H_{16}N_2)[CuCl_4]$

D−H ··· A	D−H (Å)	H ··· A (Å)	D ··· A (Å)	D−H ··· A (°)
C1−H1B...Cl29	0.99	2.75	3.726(5)	170.8
C4−H4B...Cl26	0.99	2.75	3.586(5)	141.4
N7−H7A...Cl29	0.91	2.62	3.238(4)	126.2
N7−H7A...Cl28	0.91	2.51	3.344(4)	152.2
N7−H7B...Cl27	0.91	2.72	3.316(4)	124.1
N7−H7B...Cl28	0.91	2.40	3.204(4)	147.4
C10−H10B...Cl29	0.99	2.67	3.649(5)	170.6
C10−H10B...Cl27	0.99	2.79	3.537(5)	132.7
C13−H13A...Cl27	0.99	2.77	3.653(5)	149.0
C13−H13B...Cl28	0.99	2.71	3.528(5)	140.8
N16−H16...Cl26	0.85(6)	2.41(6)	3.164(4)	147(5)
N16−H16...Cl27	0.85(6)	2.77(6)	3.412(4)	133(5)

https://doi.org/10.1021/acsomega.2c07389
ACS Omega 2023, 8, 7738−7748

Table 3. Selected Experimental and Theoretical Bond Lengths (Å) and Bond Angles (°) for $(C_6H_{16}N_2)[CuCl_4]$

band	exp	theo	band	exp	theo
distances (Å)					
C1−N16	1.497(6)	1.51227	C1−C4	1.505(7)	1.5322
C4−N7	1.490(6)	1.52704	N7−C10	0.491(6)	1.5239
C10−C13	1. 509(6)	1.52985	C13−N16	1.496(6)	1.5157
N16−C18	1.504(6)	1.53188	C18−C21	1.508(9)	1.5336
Cu25−Cl29	2.2253(13)	2.34885	Cu25−Cl26	2.2318(13)	2.5607
Cu25−Cl27	2.2638(13)	2.43997	Cu25−Cl28	2.2670(14)	2.2429
angles (°)					
N16−C1−C4	111.5(4)	111.30651	C1−N16−C18	110.4(4)	113.682
N7−C4−C1	109.4(4)	115.31497	C13−N16−C18	112.6(4)	111.477
C4−N7−C10	110.9(4)	116.56601	C13−N16−C1	110.4(4)	108.768
N7−C10−C13	111.0(4)	113.85288	N16−C13−C10	112.0(4)	109.941
N16−C18−C21	113.0(5)	112.69689	Cl27−Cu25−Cl28	95.67(5)	101.460
Cl29−Cu25−Cl26	97.52(5)	94.15286	Cl29−Cu25−Cl27	142.47(5)	109.5787
Cl26−Cu25−Cl27	95.71(5)	101.12489	Cl29−Cu25−Cl28	95.90(5)	105.0031
Cl26−Cu25−Cl28	140.75(6)	143.26344			

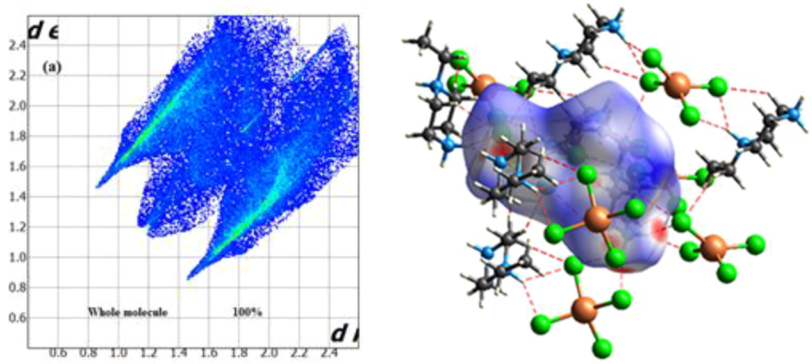

Figure 3. (a) FP plot illustrating the total percentage contribution of various interactions to HS area and (b) mapped d_{norm} quantity on Hirshfeld surface of the asymmetric unit.

Table 4. Random Contacts of Hirshfeld Surfaces and Enrichment Ratios for $(C_6H_{16}N_2)[CuCl_4]$

	H	Cl	Cu
atoms			
surface (*S* %)	62.15	34.9	1.85
contacts (*C* %)			
Cl	66.4	1.3	
H	27.1		3.7
contacts imaginaries (*R* %)			
H	38.63		0.574
Cl	1.084	12.18	
enrichment (*E*)			
E_{H}...	0.70		6.446
E_{Cl}...	61.25	0.107	

2EPCU. The intense binding observed at around 500 nm must be attributed to ligand-to-metal charge transfer; the band at 720 nm is assigned to the d−d transition of the metal ion Cu^{2+}. These findings are similar to those obtained for the hybrid material $(C_7H_{16}N_2)[CuCl_4]$,[50] in which the organic component is transparent in the UV−visible range. The TD-DFT calculation predicts two absorption bands at 420 nm and 675 nm. Diffuse reflectance spectra of poorly absorbing compounds are commonly analyzed using the Kubelka−Munk theory. The following formula represents the Kubelka−Munk reflectance function[51]

$$F(R) = (1 - R)/2R$$

R stands for the reflectance of 2EPCU, while $F(R)$ shows the Kubelka−Munk function.

Figure S5a,b exhibits the diffuse reflectance spectra and the Kubelka−Munk curve of $(C_6H_{16}N_2)[CuCl_4]$ at various wavelengths, respectively. The linear portion of the extraction must be extrapolated[53] in order to produce a band gap energy E_g = 2.10 eV utilizing the direct band gap energy of 2EPCU $[(F(R)\ h\nu)^2 = h\nu]$ from the TAUC plot approach extraction[52] (Figure 4).

The highest occupied molecular orbital (HOMO) and lowest unoccupied molecular orbital (LUMO) make up the Frontier Molecular Orbitals (FMOs). The chemical stability of molecules can be quantified by measuring the gap energy between their two orbitals. A larger gap signifies that a molecule is more stable and therefore less reactive. Figure 5 shows the computed HOMO, HOMO-1, HOMO-3, HOMO-4, HOMO-5, HOMO-6, HOMO-7, and LUMO orbitals and the gap energy in the gas phase. The red and green areas show the positive and negative phases, respectively. According to the TD-DFT approach using the B3LYP/LanL2DZ basis set, the HOMO and LUMO energy values, both equal to 2.1265 eV, are as follows: E_{HOMO} = −6.128616 eV; E_{LUMO} = −4.001664

https://doi.org/10.1021/acsomega.2c07389
ACS Omega 2023, 8, 7738−7748

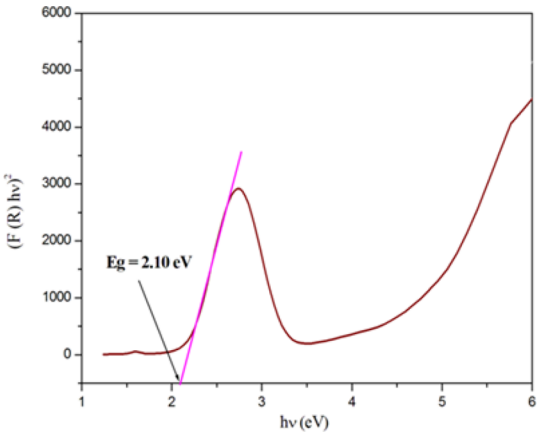

Figure 4. Energy dependence of $(F(R)\ h\nu)^2$ versus photon $(h\nu)$.

eV. The studied material exhibits a small HOMO−LUMO energy gap, indicating its semiconductor nature. In addition, the E_{HOMO} and E_{LUMO} values can also be applied to determine the chemical hardness, global softness, electron affinity, and ionization potential. Electronegativity can be calculated using either the Mulliken definition $(\chi = (I + A)/2)$ or the global chemical potential $(\mu = -(I + A)/2)$ and global electrophilicity $(\omega = \mu 2/2\eta)$ established by Parr et al.[54,55] Table 5 summarizes all calculated chemical reactivity descriptor values. The absorption spectrum was used to calculate the optical transmittance spectrum of the 2EPCU compound (Figure S6). The optical transmission range, transparency limit, and absorbance band are the three essential optical characteristics for laser frequency conversion applications for any material. Figure S6 shows that the crystal transmits 100% of visible light and that the cut-off wavelength is 439.04 nm. Due to the lack of absorption in the visible range, our crystal may be suitable for optical uses.

PL Properties. PL measurements of the title compound were carried out in the solid state at room temperature. Figure 6 illustrates the simultaneous emission and excitation spectra.

Table 5. Calculated HOMO, LUMO, Energy Values, HOMO−LUMO Energy Gap, Chemical Potential, Chemical Hardness, Electrophilicity Index, Softness, and Electronegativity of $(C_6H_{16}N_2)[CuCl_4]$

parameters	values (eV)
E_{HOMO}	−6.12816
E_{LUMO}	−4.001664
energy band gap $\lvert E_{HOMO} - E_{LUMO}\rvert$	2.1265
chemical hardness $\eta = \frac{(I-A)}{2}$	1.0632
chemical potential for the molecule $\mu = \frac{-(I+A)}{2}$	−5.0649
softness $S = \frac{1}{2\eta}$	0.4703
electrophilicity index of the molecule $W = \frac{\mu^2}{2\eta}$	12.04489
electronegativity $\chi = \frac{-(I+A)}{2}$	5.0649

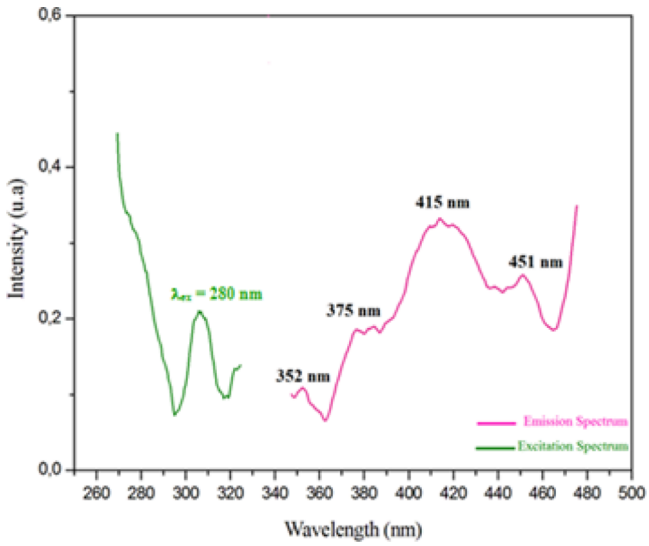

Figure 6. Emission spectra of $(C_6H_{16}N_2)[CuCl_4]$.

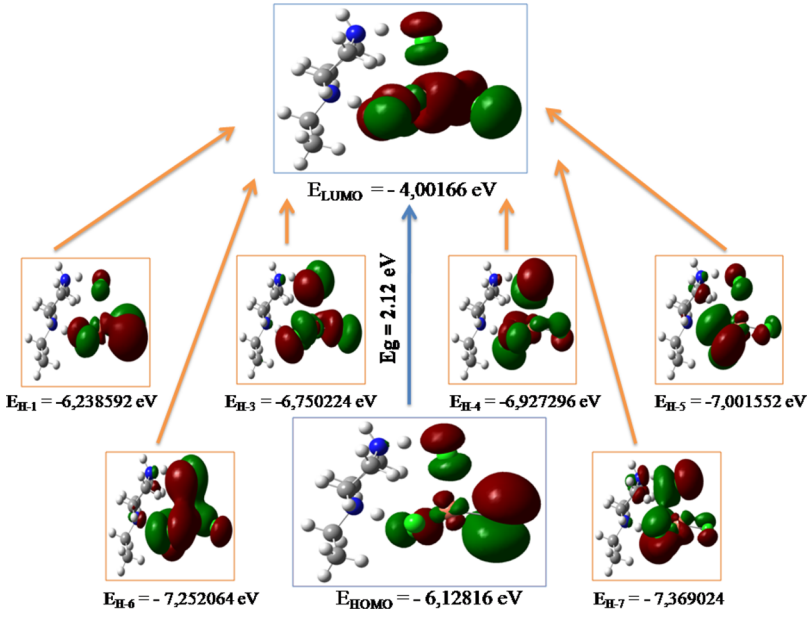

Figure 5. Molecular orbital surfaces for the HOMO, HOMO-1, HOMO-3, HOMO-4, HOMO-5, HOMO-6, HOMO-7, and LUMO.

https://doi.org/10.1021/acsomega.2c07389
ACS Omega 2023, 8, 7738−7748

There are several distinct bands in the emission spectrum upon excitation at 280 nm. The various bands observed in the PL spectrum can be attributed to excited-to-ground-state transition. The broad and intensive emission peak observed at 415 nm is due to charge transfer between the anionic groups $[CuCl_4]^{2-}$ and the organic cation $[C_6H_{16}N_2]^{2+}$, as well as the charge transfer metal to ligand (CTML). In addition, the emission wavelength at 451 nm can be attributed to the charge transfer ligand to metal. In contrast, the lowest emission bands at 375 and 352 nm indicated CTML and charge transfer anion to cation, respectively. Finally, the investigated compound exhibits violet luminescence at an excitation wavelength of 280 nm. This description agrees well with a similar compound reported in literature.[56]

NBO Analyses. The NBO study of $(C_6H_{16}N_2)[CuCl_4]$ shows that both chlorine and nitrogen are highly electronegative, resulting in high polarization coefficients (Table S2). A change in the electronic doublets within the $CuCl_4$ unit is visible in a second-order perturbation study of the Fock matrix using NBOs. This shift indicates that the chlorine atoms (Cl26 and Cl28) are transferred using one of their doublets, stabilizing the system. The perturbation energies of the donor−acceptor interaction are shown in Table S3. In the title compound $(C_6H_{16}N_2)[CuCl_4]$, the LP(4)Cl26-LP*(6)-Cu25 has 17.23 kcal.mol^{-1}, LP(4)Cl26-LP*(7)Cu25 has 16.19 kcal.mol^{-1}, LP(3)Cl28-LP*(6)Cu25 has 14.05, and LP(3)-Cl28-LP*(7)Cu25 has 12.52 kcal.mol^{-1}. Furthermore, the stabilization energies of the LP(4)Cl28−σ*(N7−H9) and LP(3)Cl26−σ*(N16−H17) interactions are 24.36 and 8.28 kcal.mol^{-1}, respectively, indicating the existence of an intermolecular N−H ···Cl hydrogen bond in 2EPCU.

Molecular Electrostatic Potential Surfaces. B3LYP was used to calculate the molecular electrostatic potential of 2EPCU. The blue color indicates the maximum positive region, susceptible to nucleophilic attack symptoms, and the red color indicates the maximum negative region, which has a higher potential to be attacked by electrophiles. The molecular electrostatic potential is useful as a measure of molecular shape and size because it reveals the presence of both negative and positive regions of electrostatic potential. Molecular electrostatic potential surface analysis identifies electron donor and electron acceptor regions that can be utilized to study intramolecular and intermolecular interactions, like hydrogen bonds. The chlorine atoms surrounding the $[CuCl_4]^{2-}$ moiety has the negative electrostatic potential of sites in 2EPCU. The electrostatic potential of the cation $[C_6H_{16}N_2]^{2+}$ is positive at the hydrogen sites of nitrogen atoms (Figure 7). The potential dispersion in $(C_6H_{16}N_2)[CuCl_4]$ is −0.116 to 0.116 a.u. These results are similar to compound $(C_{10}H_{28}N_4)$ $[CoCl_4]_2$.[57]

RDG Analyses. A wide variety of chemical, physical, and biological reactions are influenced by weak interactions.[58] There are a variety of ways to use them, including storing hydrogen for renewable energy.[59] RDG, which uses the introduced charge density as a color coding method, is commonly used to analyze weak interactions, including van der Waals contacts, repulsive interactions, or hydrogen bonds.[60,61] Figure 8a,b, generated with the VMD and Multiwfn programs, illustrates the non-covalent interactions between molecules of $(C_6H_{16}N_2)[CuCl_4]$.[62,63] A graph of the RDG function versus electron density ρ multiplied by the sign of the second eigenvalue of λ_2 2EPCU is shown in Figure 8b. In this figure, we can distinguish different interaction regions using a color code in this figure; color-coded areas indicate the type of

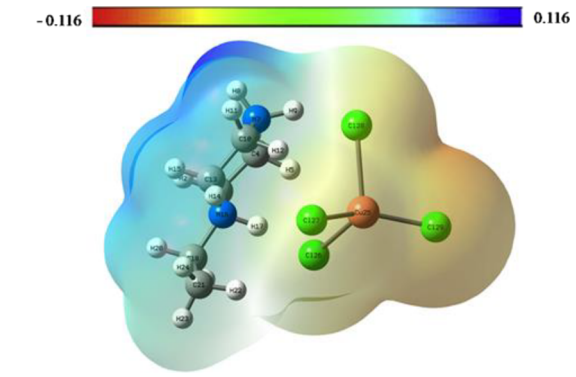

Figure 7. Molecular electrostatic potential surface (−0.0116 to 0.116) of $(C_6H_{16}N_2)[CuCl_4]$.

interaction. An attractive interaction occurs when $(\lambda_2)\rho$ has a negative value (blue color). For example, the van der Waals interaction is observed when sign $(\lambda_2)\rho$ approaches zero (green), while when the sign $(\lambda_2)\rho$ is positive (red), strong repulsive interactions are observed. Furthermore, van der Waals interactions are attributed to the light brown and green plates between the anionic and cationic units, while repulsive interactions are ascribed to the elliptical red plate found in $[CuCl_4]$.[2] An image of the blue spot formed when a hydrogen atom is paired with a nitrogen atom and a chloride atom, demonstrating the presence of an attraction between N−H ··· Cl.

QTAIM Analysis. The QTAIM technique is a powerful approach for determining the existence of critical points (CPs) used to identify chemical bonds and interatomic interactions. To evaluate the characteristics of the bonds, specifically the hydrogen bonds, the program Multiwfn may calculate the topological parameters at a CP of the bond, namely, electron density $\rho(r)$, Laplacian values $\nabla 2\rho(r)$, and ellipticity (ε).[63,64] However, the latter can be classified as strong or extremely strong hydrogen bonds when $\nabla_2\rho(r_{BCP}) < 0$ and $H(r_{BCP}) < 0$, moderate hydrogen bonds when $\nabla_2\rho(r_{BCP}) > 0$ and $H(r_{BCP}) < 0$, and weak hydrogen bonds, when $\nabla_2\rho(r_{BCP}) > 0$ and $H(r_{BCP}) > 0$.[65] QTAIM, at variance, fails to diagnose the different nature of the H...H interaction.[66] Figure S7 depicts the analysis of the 2EPCU compound using the QTAIM method, whereas Table 6 displays the calculated topological parameters. The topological analysis of the QTAIM shows that two hydrogen bonds N−H ···Cl stabilize the 2EPCU compound. The BCP analysis in Table 2 reveals that the only hydrogen bond is N−H9···Cl28, which possesses an energy of −4.033 kcal.mol^{-1} and a density of electrons equal to 0.8926×10^{-2} a.u. These results demonstrate that, in contrast to other compounds, the title compound exhibits strong hydrogen bonding.[67,68] The Rozas criterion indicates that these values exceeded zero. Furthermore, QTAIM analysis detects the existence of new RCP and NRCP cycles at the critical ring point, established by hydrogen bonding interactions in 2EPCU. Our investigations reveal that the title compound exhibits H−H Pauli repulsion rather than H−H bonding.

Thermal Studies. The thermogravimetry differential thermal analysis for the $(C_6H_{16}N_2)[CuCl_4]$ compound was performed in an argon atmosphere at a heating rate of 5 °C min^{-1} between 25 and 700 °C (Figure S8). The release of a hydrochloric acid molecule is attributed to the first endothermic peak at 210 °C. The experimental mass loss (11.27%) and the estimated mass loss (11.35%) are in good

https://doi.org/10.1021/acsomega.2c07389
ACS Omega 2023, 8, 7738−7748

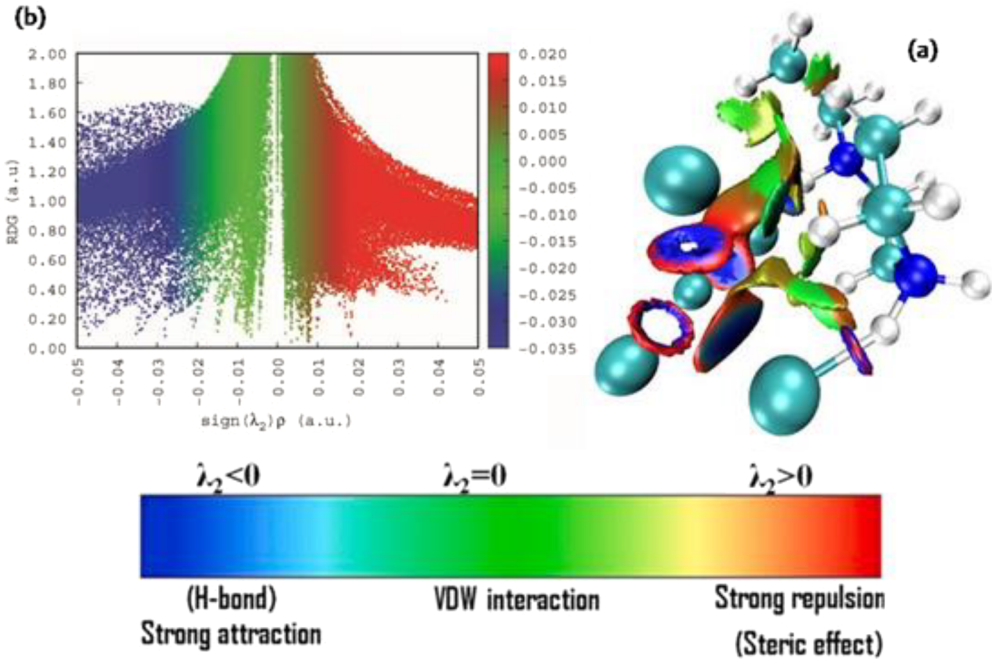

Figure 8. Reduced density gradient (a) and isosurface density (b) plot, combined with the color-filled scale bar, defining the limits of interaction for the 2EPCU compound.

Table 6. Topological Parameters for the $(C_6H_{16}N_2)[CuCl_4]$ Compound[a]

bond	D (Å)	$\rho(r)$ (a.u)	$\nabla^2\rho(r)$ (a.u)	$V(r)$ (a.u)	E_{int} (kcal.mol^{-1})	(ε)	(ζ)
H9 ... Cl28	1.9056	0.8926×10^{-2}	0.2986×10^{-1}	-0.52097×10^{-2}	−4.033	0.9508	0.148
RCP		0.523×10^{-2}	0.1707×10^{-1}	-0.23864×10^{-2}		0.1947	0.154
NRCP		0.8926×10^{-2}	0.2986×10^{-1}	$-0.19228 \times 10^{+1}$		0.0007	−1.0853

[a]D (Å): distance; $\rho(r)$ (a.u.): density of electrons; $\nabla^2\rho(r)$ (a.u): Laplacian of electron density; $V(r)$ (a.u): potential energy density; (E_{int}) (kJ.mol^{-1}): interaction energy; (ε): ellipticity; (ζ): eta index, RCP: ring critical point and NRCP: new ring critical point.

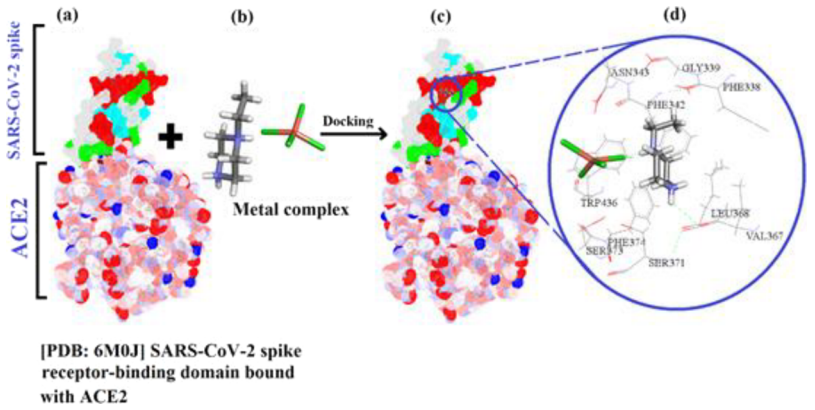

Figure 9. (a) Crystal structure of SARS-CoV-2 spike receptor-binding domain bound with ACE2, (b) copper complex as a ligand, (c) best receptor binding domain-ligand complex binding pose, and (d) 2D interaction map indicates the major participating amino acid in the binding pocket.

agreement. The mass loss observed experimentally (11.30%) is extremely close to the mass loss calculated (11.35%), indicating that the release of the second molecule of hydrochloric acid is due to a series of small endothermic peaks, the most significant of which occurs around 285 °C. Finally, the decomposition or combustion of the organic part is indicated by an endothermic peak near 360 °C and a series of exothermic peaks, the most significant of which is at 460 °C. Finally, the experiment shows that mass loss has taken place when black powder and $CuCl_2$ are combined. Several thermochemical characteristics, including rotational temperatures and constants, entropy, zero-point energy, thermal energy, enthalpy, heat capacity, and Gibbs free energy of molecular systems, can also be determined utilizing the Gaussian software. The thermochemical characteristics are shown in Table S4.

Using the equation, the corrected enthalpy term (ΔH) associated with the total energy of the system can be determined.

$$H_{corr.} = E_{total} + k_b \times T$$

https://doi.org/10.1021/acsomega.2c07389
ACS Omega 2023, 8, 7738−7748

ΔH in $(C_6H_{16}N_2)[CuCl_4]$ was determined to be 0.257024 Hartree/particle. The vibrational energy of $(C_6H_{16}N_2)[CuCl_4]$ at zero points was calculated to be 149.33456 kcal.mol^{-1}. The corrected total electronic energy, E_{total} + ZPE_{corr}, was calculated to be −603.569556 a.u. The values determined for thermal energy, heat capacity, and entropy were 160.693, 60.206, and 143.071 kcal.mol^{-1}, respectively. As a result, entropy has a significant effect on the reactivity of 2EPCU. Finally, this finding emphasizes the significance of vibration analysis studies of molecular systems.

Antioxidant Study. $DPPH^{\cdot+}$ radical and $ABTS^{\cdot+}$ radical cation assays are commonly used to determine antioxidant activity. The $DPPH^{\cdot+}$ scavenger properties showed the same relationships as the $ABTS^{\cdot+}$ method. The observed $DPPH^{\cdot+}$ scavenging capacity reached up to 24.19% ±3.3 at10 mg.mL^{-1} and 47.71% ± 0.5 at 50 mg.mL^{-1}. The $ABTS^{\cdot+}$ test showed a higher percentage of inhibition 51.31% ± 2.28 at 50 mg.mL^{-1}. However, in both tests, the IC_{50} of the sample was greater than 45 mg.mL^{-1} as shown in Figure S9.

Molecular Docking Analyses. The receptor-binding region of the SARS-CoV-2 spike is an essential component for viral entrance into the host cell because of its interaction with the ACE2 receptor. Recent findings on the X-ray crystal structure of the SARS-CoV-2 spike receptor have opened up the prospect of developing medications to block viral entry into the host cell by targeting the SARS-CoV-2 spike receptor-binding domain based on the receptor's amino acid sequence. As illustrated by Discovery studio, the active binding site of the SARS-CoV-2 spike structure was built around amino acids like ASN 343, PHE 338, GLY 339, VAL 367, LEU 368, SER 371, PHE 374, SER 373, and TRP 436. The best docking pose with −30.87 S (PLP) was chosen from among the hierarchy poses of spike protein and complex for the mechanistic approach of nonbinding interactions, as depicted in Figure 9. A stable complex is formed when the complex makes a hydrogen bond with VAL 367, an amino acid residue in a spike, at a distance of 2.40 Å. The spike receptor binding amino acid residues such as GLY 339, PHE 338, LEU 368, PHE 374, and TRP 436 were found to have hydrophobic interactions with a hybrid inorganic−organic. As seen in the figure, these active amino acids of the SARS-CoV-2 spike receptor formed a deep ring around the complex in such a way as to deepen the persistent receptor−complex receptor interactions. Based on the various hydrophilic and hydrophobic interacting mechanisms, including the hydrogen bond of the active amino acid of the spike receptor with a hybrid inorganic−organic compound, these involvements may be damaging to virus transmission, but more research on metal complexes against receptor is needed to prove their significance in preventing virus spread. In addition, we have also made a comparison of copper complexes reported in the literature with numerous spike proteins using different software of molecular docking techniques (Table S5). The results of the inhibitory activity are similar to previous studies on the copper complexes.[69−73]

CONCLUSIONS

We successfully investigated a new non-centrosymmetric compound $(C_6H_{16}N_2)[CuCl_4]$ at room temperature. The optical properties of this material were studied, and the energy gap was found to be 2.12 and 2.10 eV, respectively, by experimental and theoretical calculations. The NBO study of the title compound revealed that the intermolecular interactions N−H···Cl significantly affect packing in this system. QTAIM analysis was utilized to show the H···H interactions found in the Hirshfeld surface analysis and to indicate the existence of cycles in a molecular system. Furthermore, the antioxidant activity of the title compound demonstrated excellent scavenging of radicals in $DPPH^{\cdot+}$ radical and $ABTS^{\cdot+}$ radical cation tests. The findings revealed that their effect occurred in a concentration-dependent manner.

ASSOCIATED CONTENT

Supporting Information

The Supporting Information is available free of charge at https://pubs.acs.org/doi/10.1021/acsomega.2c07389.

2D FP plots; comparative FT-IR spectra; correlation graph (cm^{-1}); correlation graph (nm); diffuse reflectance spectra; Kubelka−Munk absorption spectra; optical transmittance spectrum; AIM analysis; thermogravimetric analyses; scavenging activity; IR vibrational modes; NBO; second-order perturbation theory analysis; computed thermo-chemical features; and molecular docking techniques (PDF)

AUTHOR INFORMATION

Corresponding Authors

Mohammad Azam − *Department of Chemistry, College of Science, King Saud University, Riyadh 11451, Saudi Arabia;* orcid.org/0000-0002-4274-2796; Email: azam_res@yahoo.com, mhashim@ksu.edu.sa

Riadh Kefi − *Laboratoire de Chimie des Matériaux, Faculté des Sciences de Bizerte, Université de Carthage Faculté des Sciences de Bizerte, 7021 Zarzouna, Tunisie;* orcid.org/0000-0002-9871-302X; Email: riadhkef@yahoo.fr

Authors

Afef Gannouni − *Laboratoire de Chimie des Matériaux, Faculté des Sciences de Bizerte, Université de Carthage Faculté des Sciences de Bizerte, 7021 Zarzouna, Tunisie*

Wiem Tahri − *Laboratory of Biochemistry and Molecular Biology, Faculty of Sciences, Risks Related to Environmental Stress, Struggle and Prevention (UR17ES20), University of Carthage, Te Ministry of Higher Education and Scientific Research, Zarzouna, 7003 Bizerte, Tunisia*

Thierry Roisnel − *Université Rennes, CNRS, ISCR (Institut des Sciences Chimiques de Rennes) − UMR 6226, F-35000 Rennes, France*

Saud I. Al-Resayes − *Department of Chemistry, College of Science, King Saud University, Riyadh 11451, Saudi Arabia*

Complete contact information is available at: https://pubs.acs.org/10.1021/acsomega.2c07389

Notes

The authors declare no competing financial interest.

ACKNOWLEDGMENTS

The authors acknowledge the financial support through Researchers Supporting Project number (RSP2023R147), King Saud University, Riyadh, Saudi Arabia.

REFERENCES

(1) Hachani, A.; Dridi, I.; Othmani, A.; Roisnel, T.; Humbel, S.; Kefi, R. A zero-dimensional hybrid organic-inorganic perovskite $CuCl_4$ based: synthesis, crystal structure, vibrational, optical proper-

ties, DFT and TDFT calculations, dielectric properties and biological activity. *J. Mol. Struct.* **2021**, *1229*, No. 129838.
(2) Kessentini, A.; Belhouchet, M.; Sunol, J. J.; Abid, Y.; Mhiri, T. Crystal structure, vibrational studies and optical properties of a new organic−inorganic hybrid compound $(C_{10}H_{28}N_4)CuCl_5Cl_4H_2O$. *Spectrochim. Acta, Part A* **2015**, *134*, 28.
(3) Arularasan, P.; Sivakumar, B.; Chakkaravarthi, G.; Mohana, R. Bis([mu]-L-arginine-[kappa]$_3$N$_2$,O:O′)bis(L-arginine-[kappa]$_2$N$_2$,O)tetra-[mu]-chlorido-tetrachloridotetracopper(II). *Acta Crystallogr., Sect. E: Struct. Rep. Online* **2013**, *69*, 583.
(4) Dammak, T.; Boughzala, H.; Mlayah, A.; Abid, Y. Elaboration, structural, vibrational and optical investigation of a two-dimensional self-assembled organic−inorganic hybrid compound. *J. Lumin.* **2016**, *173*, 213−217.
(5) Al-Far, R. H.; Ali, B. F. The Crystal Structures of Bis (2-amino-5 methylpyridinium) Tetrabromometallate (II): Intermolecular Interactions in $(C_6H_9N_2)_2$ [MBr_4]; M = Cd and Co. *J. Chem. Crystallogr.* **2008**, *38*, 373.
(6) Sorenson, J. R. J. Copper chelates as possible active forms of the antiarthritic agents. *J. Med. Chem.* **1976**, *19*, 135.
(7) Englebienne, P.; Hoonacker, A. V. Gold−conductive polymer nanoparticles: A hybrid material with enhanced photonic reactivity to environmental stimuli. *J. Colloid Interface Sci.* **2005**, *292*, 445−454.
(8) Müller, A.; Reuter, H.; Dillinger, S. Supramolecular inorganic chemistry: small guests in small and large hosts. *Angew. Chem., Int. Ed. Engl.* **1995**, *34*, 2328−2361.
(9) Li, Y.; Yu, Y.; Wu, L.; Zhi, J. Processable polyaniline/titania nanocomposites with good photocatalytic and conductivity properties prepared via peroxo-titanium complex catalyzed emulsion polymerization approach. *Appl. Surf. Sci.* **2013**, *273*, 135−143.
(10) Gribble, G. K.; Saulnier, M. G.; Sibi, M. P.; Obaza-Nutaitis, J. A. Synthesis and Diels-Alder reactions of 1, 3-dimethyl-4-(phenylsulfonyl)-4H-furo [3, 4-b] indole. *J. Org. Chem.* **1984**, *49*, 4518−4523.
(11) Müller, A.; Peters, F.; Pope, M. T.; Gatteschi, D. Polyoxometalates: very large clusters-nanoscale magnets. *Chem. Rev.* **1998**, *98*, 239−272.
(12) Novena, L. M.; Kumar, S. S.; Athimoolam, S. Improved solubility and bioactivity of theophylline (a bronchodilator drug) through its new nitrate salt analysed by experimental and theoretical approaches. *J. Mol. Struct.* **2016**, *1116*, 45−55.
(13) Braun, P. V.; Osenar, P.; Tohver, V.; Kennedy, S. B.; Stupp, S. I. Nanostructure templating in inorganic solids with organic lyotropic liquid crystals. *J. Am. Chem. Soc.* **1999**, *121*, 7302−7309.
(14) Daniel, M. C.; Astruc, D. Gold nanoparticles: assembly, supramolecular chemistry, quantum-size-related properties, and applications toward biology, catalysis, and nanotechnology. *Chem. Rev.* **2004**, *104*, 293−346.
(15) Humle, C.; Cheerier, M. P. Novel applications of ethyl glyoxalate with the Ugi MCR. *Tetrahedron Lett.* **1999**, *40*, 5295−5299.
(16) Gatfaoui, S.; Mezni, A.; Roisnel, T.; Marouani, H. Synthesis, characterization, Hirshfeld surface analysis and antioxidant activity of a novel organic-inorganic hybrid material 1-methylpiperazine-1, 4-diium bis (nitrate). *J. Mol. Struct.* **2017**, *1139*, 52−59.
(17) Gatfaoui, S.; Issaoui, N.; Mezni, A.; Bardak, F.; Roisnel, T.; Atac, A.; Marouani, H. Synthesis, structural and spectroscopic features, and investigation of bioactive nature of a novel organic-inorganic hybrid material 1*H*-1,2,4-triazole-4-ium trioxonitrate. *J. Mol. Struct.* **2017**, *1150*, 242−257.
(18) Kozak, J. J.; Gray, H. B.; Garza-López, R. A. Structural stability of the SARS-CoV-2 main protease: Can metal ions affect function. *J. Inorg. Biochem.* **2020**, *211*, No. 111179.
(19) Lan, L.; Ge, J.; Shan, S.; Zhou, H.; Fan, S.; Zhang, Q.; Shi, X.; Wang, Q.; Zhang, L.; Wang, X. Structure of the SARS-CoV-2 spike receptor-binding domain bound to the ACE2 receptor. *Nature* **2020**, *581*, 215−220.
(20) Garza-López, R. A.; Kozak, J. J.; Gray, H. B. Copper (II) inhibition of the SARS-CoV-2 main protease. *ChemRxiv* **2020**, 33200118.
(21) Chaturvedi, U. C.; Shrivastava, R. Interaction of viral proteins with metal ions: role in maintaining the structure and functions of viruses. *FEMS Immunol. Med. Microbiol.* **2005**, *43*, 105−114.
(22) Sheldrick, G. M. *SHELXT* − Integrated space-group and crystal-structure determination. *Acta Crystallogr., Sect. A: Found. Adv.* **2015**, *71*, 3−8.
(23) Sheldrick, G. M. Crystal structure refinement with SHELXL. *Acta Crystallogr., Sect. C: Struct. Chem.* **2015**, *71*, 3−8.
(24) Brandenburg, K. *Diamond Version 2.0 Impact GbR*; Bonn, Germany, 1998.
(25) Lee, C.; Yang, W. W.; Parr, R. G. Development of the Colle-Salvetti correlation-energy formula into a functional of the electron density. *Phys. Rev. B* **1988**, *37*, 785−789.
(26) Becke, D. A new mixing of Hartree−Fock and local density-functional theories. *J. Chem. Phys.* **1993**, *98*, 5648−5652.
(27) Parr, R. G.; Wang, W. *Section 3 of density-functional theory of atoms andmolecules*; Oxford University Press: New York, 1989.
(28) Frisch, M. J.; Trucks, G. W.; Schlegel, H. B.; Scuseria, G. E.; Robb, M. A.; Cheeseman, J. R.; Scalmani, G.; Barone, V.; Mennucci, B.; Petersson, G. A.; et al. *Gaussian 09, Revision A.1*, Gaussian, Inc.: Wallingford CT, 2009.
(29) Jamroz, M. H. *Vibrational Energy Distribution Analysis: VEDA 4 Program*, Warsaw, Poland, 2004. http://www.smmg.pl.
(30) Thuy, B. T. P.; My, T. T. A.; Hai, N. T. T.; Hieu, L. T.; Hoa, T. T.; Loan, H. T. P.; Triet, N. T.; Van Anh, T. T.; Quy, P. T.; Van Tat, P.; et al. Investigation into SARS-CoV-2 Resistance of Compounds in Garlic Essential Oil. *ACS Omega* **2020**, *5*, 8312−8320.
(31) Dhieb, A. C.; Dridi, I.; Mathlouthi, M.; Rzaigui, M.; Smirani, W. Structural physico chemical studies and biological analyses of a cadmium cluster complex. *J. Cluster Sci.* **2018**, *29*, 1123−1131.
(32) Guesmi, F.; Ben Farhat, M.; Mejri, M.; Landoulsi, A. In-vitro assessment of antioxidant and antimicrobial activities of methanol extracts and essential oil of Thymus hirtus sp algeriensis. *J. Lipids Health Dis.* **2014**, *13*, 114.
(33) Essghaier, H.; Barea, B.; Sadfi-Zouaoui, E.; Zid, M. F. Synthesis, structural study, magneticsusceptibility and antimicrobialactivity of the first (μ-oxo)-bis(oxalato)-vanadium(IV) 1D coordination polymer. *J. Mol. Struct.* **2019**, *1175*, 865−873.
(34) Halvorson, K. E.; Patterson, C.; Willett, R. D. Patterson, Willett CRD Structures of bis (4-aminopyridinium) tetrachlorocuprate (II) monohydrate,$[C_5H_7N_2]_2[CuCl_4].H_2O$ and bis (2-amino-3-hydroxypyridinium) tetrachlorocuprate (II). *Acta Crystallogr., Sect. B* **1990**, *46*, 508−519.
(35) Baur, W. Straight Si-O-Si bridging bonds do exist in silicates and silicondioxide polymorphs. *Acta Crystallogr., Sect. B* **1980**, *36*, 2198−2202.
(36) Zanchini, C.; Willett, R. D. Crystal structure, magnetism, and electronic and EPR spectroscopies of bis(2-aminopyrimidinium)-tetrachlorocuprate(II): a square-planar $CuCl_4^{2-}$ anion with semi-coordinated cationic ligands. *Inorg. Chem.* **1990**, *29*, 3027−3030.
(37) Yang, L.; Powell, D. R.; Houser, R. P. Structural variation in copper (I) complexes with pyridylmethylamide ligands: structural analysis with a new four-coordinate geometry index, τ4. *Daltons Trans.* **2007**, *9*, 955−964.
(38) Mkaouar, I.; Karâa, K.; Hamdi, B.; Zouari, R. Synthesis, crystal structure, thermal analysis, vibrational study dielectric behaviour and Hirshfeld surface analysis of $[C_6H_{10}\ (NH_3)_2)]_2SnCl_6(Cl)_2$. *J. Mol. Struct.* **2016**, *1115*, 161−170.
(39) Mkaouar, I.; Hamdi, B.; Karaa, N.; Zouari, R. Synthesis, solid-state characterization and dielectric properties of a trichlorostanate (II) complex. *J. Polyhedron* **2015**, *87*, 424−432.
(40) Arbi, M.; Khedhiri, L.; Wojtas, M.; Jeanneau, E.; Lefebvre, F.; Ben Nasr, C. Synthesis and characterization of two organic cation hydrogensulfates: 1- (2,5-dimethylphenyl) piperazine-1,4-diium bis (hydrogensulfate) monohydrate (SI) and 1-(2,3-dimethylphenyl)-piperazine-1,4-diium bis(hydrogensulfate) (SII). *J. Mol. Struct.* **2017**, *1134*, 625−637.
(41) Cremer, D.; Pople, J. A. General definition of ring puckering coordinates. *J. Am. Chem. Soc.* **1975**, *97*, 1354.

https://doi.org/10.1021/acsomega.2c07389
ACS Omega 2023, 8, 7738−7748

(42) Mckinnon, J. J.; Spackman, M. A.; Mitchell, A. S. Novel tools for visualizing and exploring intermolecular interactions in molecular crystals. *Acta Crystallogr., Sect. B* **2004**, *60*, 627−668.
(43) Mckinnon, J. J.; Jayatilaka, D.; Spackman, M. A. Towards quantitative analysis of intermolecular interactions with Hirshfeld surfaces. *J. Chem. Commun.* **2007**, *37*, 3814−3816.
(44) Tounsi, A.; Elleuch, S.; Hamdi, B.; Zouari, R.; Ben Salah, A. Structural study, Hirshfeld surface analysis, spectroscopic properties and DFT investigation of a new hybrid compound: $(C_6H_{10}(NH_3)_2)_3[CoCl_4](Cl)_4.3H_2O$. *J. Mol. Struct.* **2017**, *1141*, 512−523.
(45) Yusof, E. N. M.; Jotani, M. M.; Tiekink, E. R. T.; Ravoof, T. B. S. A. 2-[(1E) ({[(Benzylsulfanyl)methanethioyl]amino}imino)-methyl]-6-methoxyphenol: crystal structure and Hirshfeld surface analysis. *Acta Crystallogr., Sect. E: Crystallogr. Commun.* **2016**, *72*, 516−521.
(46) Jelsch, C.; Ejsmont, K.; Huder, L. The enrichment ratio of atomic contacts in crystals, an indicator derived from the Hirshfeld surface analysis. *IUCrJ.* **2014**, *1*, 119−128.
(47) Gannouni, A.; Tahri, W.; Thierry, R.; Kefi, R. X-ray diffraction, IR spectrum, optical properties, AIM, NBO, RDG, HS, Fukui function, biological and molecular docking analysis of a novel hybrid compound $(C_9H_{15}N_3)[CuCl_4(H_2O)]$. *J. Mol. Struct.* **2023**, *1271*, No. 134094.
(48) Hamdi, M.; Oueslati, A.; Chaabane, I.; Hlel, F. Characterization and Electrical Properties of $[C_6H_9N_2]_2CuCl_4$ Compound, International Scholarly Research Network. *ISRN Condens. Matter Phys.* **2012**, *2012*, No. 750497.
(49) Xiao, Z.-L.; Chen, H.-Z.; Shi, M.-M.; Wu, G.; Zhou, R.-J.; Yang, Z.-S.; Wang, M.; Tang, B.-Z. *J. Mater. Sci. Eng. B* **2005**, *117*, 313−316.
(50) Sadok, I. B. H.; Hajlaoui, F.; Karoui, K.; Audebrand, N.; Thierry, R.; Zouari, N. Crystal structure, phase transitions, optical and electrical properties in a new Cu-halide organic-inorganic hybrid. *J. Mol. Struct.* **2019**, *1186*, 118−126.
(51) Dang, Y.; Yang, L.; Youxuan, S.; Dongsheng, Y.; Xiaolong, L.; Weiqun, L.; Guangfeng, L.; Haibing, X.; Xutang, T. Bulk crystal growth of hybrid perovskite material $CH_3NH_3PbI_3$. *CrystEngComm* **2015**, *17*, 665−670.
(52) Tauc, J. Optical properties and electronic structure of amorphous Ge and Si. *J. Mater. Res. Bull.* **1968**, *3*, 37−46.
(53) Kessentini, A.; Belhouchet, M.; Abid, Y.; Minot, C.; Mhiri, T. Crystal structure, vibrational studies, optical properties and DFT calculation of bis 2-aminobenzothiazolium tetrachloridocuprate. *Spectrochim. Acta, Part A* **2014**, *122*, 476−481.
(54) Mulliken, R. S. A new electroaffinity scale; together with data on valence states and on valence ionization potentials and electron affinities. *J. Chem. Phys.* **1934**, *2*, 782−793.
(55) Parr, R. G.; Von Szentpály, L.; Liu, S. Electrophilicity index. *J. Am. Chem. Soc.* **1999**, *121*, 1922−1924.
(56) Mtioui-Sghaier, O.; Mendoza-Merono, R.; Fereandez-Zapico, E.; Garcia-Granda, S.; Fernandes-Gonzalez, A.; Ktari, L.; Dammak, M. Synthesis of a new Cd(II)−Ni(II) hetero-metallic coordination polymer base on citricacid ligand X-ray structure, thermal stability, XPS and fluorescence studies. *J. Mol. Strcuct.* **2016**, *1105*, 105−111.
(57) Gannouni, A.; Dridi, I.; Elleuch, S.; Jouffret, L.; Kefi, R. Synthesis and characterization of a hybrid material $(C_{10}H_{28}N_4)$-$[CoCl_4]_2$ using Hirshfeld surface, vibrational and optical spectroscopy DFT calculations and biological activities. *J. Mol. Struct.* **2022**, *1250*, No. 131804.
(58) Autumn, K.; Sitti, M.; Liang, Y. A.; Peattie, A. M.; Hansen, W. R.; Sponberg, S.; Kenny, T. W.; Fearing, R.; Israelachvili, J. N.; Full, R. J. Evidence for van der Waals adhesion in gecko setae. *Proc. Natl. Acad. Sci. U. S. A* **2002**, *99*, 12252−12256.
(59) Dillon, A. C.; Jones, K. M.; Bekkedahl, T. A.; Kiang, C. H.; Bethune, D. S.; Heben, M. Storage of hydrogen in single-walled carbon nanotubes. *Nature* **1997**, *386*, 377.
(60) Johnson, E. R.; Keinan, S.; Mori-Sánchez, P.; Contreras-García, J.; Cohen, A. J.; Yang, W. Revealing Non covalent Interactions. *J. Am. Chem. Soc.* **2010**, *132*, 6498−6506.
(61) Contreras-Garcia, J.; Yang, W.; Johnson, E. R. Analysis of Hydrogen-Bond Interaction Potentials from the Electron Density: Integration of Non covalent Interaction Regions. *J. Phys. Chem. A* **2011**, *115*, 12983−12990.
(62) Humphrey, W.; Dalke, A.; Schulten, K. VMD: Visual molecular dynamics. *J. Mol. Graphics* **1996**, *14*, 33−38. and 27−8,
(63) Chen, T.; Lu, F. Multiwfn: a multifunctional wave function analyzer. *J. Comput. Chem.* **2012**, *33*, 580−592.
(64) Bader, R. F. W. *Atoms in Molecules: A Quantum Theory*; Oxford University Press: Oxford, 1990; p 0198558651.
(65) Rozas, I.; Alkorta, I.; Elguero, J. Behavior of Ylides Containing N, O, and C Atoms as Hydrogen Bond Acceptors. *J. Am. Chem. Soc.* **2000**, *122*, 11154−11161.
(66) Poater, J.; Sol, M.; Matthias Bickelhaupt, F. A Model of the Chemical Bond Must Be Rooted in Quantum Mechanics, Provide Insight, and Possess Predictive Power. *Chem. − Eur. J.* **2006**, *12*, 2902−2905.
(67) Doghar, C.; Issaoui, N.; Thierry, R.; Dorcet, V. Screening of potential drug from Azadirachta Indica (Neem) extracts for SARS-CoV-2: An insight from molecular docking and MD-simulation studies. *J. Mol. Struct.* **2021**, *1227*, No. 129820.
(68) Vener, M. V.; Egorova, A. N.; Churakov, A. V.; Tsirelson, V. G. Intermolecular Hydrogen Bond Energies in Crystals Evaluated Using Electron Density Properties: DFT Computations with Periodic Boundary Conditions. *J. Comput. Chem.* **2012**, *33*, 2303.
(69) Viola; Muhammad, N.; Khan, I.; Zafar, A.; Mohammad, I.; Shaukat, S.; Saqib, A.; Muhammad, I.; Rehman, S.; Khan, G. S.; et al. Synthesis, characterization, antioxidant, antileishmanial, anticancer, DNA and theoretical SARS-CoV-2 interaction studies of copper (II) carboxylate complexes. *J.Mol. Struct.* **2022**, *1253*, No. 132308.
(70) Mohan, B.; Choudhary, M. Synthesis, crystal structure, computationalstudy and anti-virus effect of mixed ligand copper (II) complex with ONS donor Schiff base and 1, 10-phenanthroline. *J. Mol. Struct.* **2021**, *1246*, No. 131246.
(71) Mohan, B.; Muhammad, S.; Al-Sehemi, A. G.; Bharti, S.; Kumar, S.; Choudhary, M. Synthesis of Copper (II) Coordination Complex, Its Molecular Docking and ComputationalExploration for Novel Functional Properties: A Dual Approach. *ChemistrySelect* **2021**, *6*, 738−745.
(72) Aggarwal, N.; Maji, S. Potential applicability of Schiff bases and theirmetal complexes during COVID-19 pandemic − a review. *Rev. Inorg. Chem.* **2022**, *42*, 363.
(73) Karges, J.; Cohen, S. M. Metal Complexes as Antiviral Agents for SARS-CoV-2. *ChemBioChem* **2021**, *22*, 2600−2607.

https://doi.org/10.1021/acsomega.2c07389
ACS Omega 2023, 8, 7738−7748